TÜBİTAK

Turkish Journal of Chemistry

http://journals.tubitak.gov.tr/chem/

Research Article

Turk J Chem
(2022) 46: 1694-1701

doi:10.55730/1300-0527.3472

Ytterbium oxide nanofibers: fabrication and characterization for energy applications

Adem SARILMAZ*
Department of Metallurgical and Materials Engineering, Faculty of Engineering, Karamanoğlu Mehmetbey University, Karaman, Turkey

Received: 28.03.2022 • **Accepted/Published Online:** 15.08.2022 • **Final Version:** 05.10.2022

Abstract: Metal oxide nanomaterials are widely used in many applications of renewable energy. Ytterbium oxide (Yb_2O_3) also attracts attention due to its similar structure to ZnO (~3,26 eV) and TiO_2 (~3,36 eV) in terms of bandgap energy. In this study, Yb_2O_3 belonging to the lanthanide oxide family was produced as nanofiber forms by using the electrospinning technique, which allows for large-scale production, for the first time. The morphological, structural, optical, and phase properties of the produced nanofibers were investigated via XRD, SEM-Mapping, TEM, FTIR, UV-Vis, and XPS characterization techniques. As a result of these analyses, it was determined that the Yb_2O_3 nanofibers with a diameter of 125 ± 15 nm have a cubic crystal structure and a bandgap of 3.32 eV. The results of this study have shown that the Yb_2O_3 nanofibers are capable of performing performance evaluations in many different energy conversion applications and others.

Key words: Yb_2O_3, ytterbium oxide, nanofiber, electrospinning, band-gap calculation

1. Introduction

The energy needs of humanity have increased in parallel with the growth of the earth's population. In the last century, the scientific world has focused on identifying environmentally friendly new alternative energy sources due to reasons such as limited fossil fuel sources and damage of these fuels to nature. When the developments in this context are examined, it is seen that the performed studies are focused on energy production from natural and renewable sources such as the sun, wind, and water. As it is known, metal oxide materials are extensively used in energy production from renewable energy sources. Literature review shows that ytterbium oxide and ytterbium-doped metal oxide nanomaterials belonging to the lanthanide oxide family are interesting materials within the scope of these studies [1-6]. For example, it has been reported in many studies that ytterbium-based or ytterbium-doped oxides increase photoactivity in hydrogen evolution reactions (HER) [3, 5, 7-9]. In addition to HER studies, these materials have been used as photoanode in dye-sensitized solar cells (DSSCs) and as upconverted layers in thin-film solar cells. It has been reported in the DSSC study that when ytterbium-based materials are used together with photoanodes such as TiO_2 and ZnO, they facilitate charge transport and increase the lifetime of photoexcited electrons [1, 6]. On the other hand, they help to absorb shorter wavelengths and thus increase the power conversion efficiency in the thin-film solar cell [10].

As can be understood from the previous studies, nanostructured Yb_2O_3 can be produced in different morphologies with various synthesis methods such as hydrothermal [11-13], solvothermal [14], precipitation [15, 16], and electrospinning [17]. Among the synthesis methods, electrospinning which is an environmentally friendly, low-cost, and simple production method is a common production technique used in nanomaterials production. This production technique generally consists of four main components: the high voltage power supply, syringe with a metal needle, syringe pump, and sample collector. The voltage range, the distance between the syringe with the collector, and feed rate are the main parameters for nanofiber production. The changes in these parameters allow the morphological properties of the produced nanofibers to be controlled. Therefore, electrospinning facilitates the production of nanofibers with porous, high aspect ratio, and large surface area. As it is known, the morphological properties of the produced materials are an important parameter for energy applications. These properties of nanofibers contribute to increasing efficiency in energy applications [18, 19]. As mentioned at the beginning of the paragraph, the synthesis routes of nanostructured Yb_2O_3 are limited, and it was reported that Yb_2O_3 was produced by electrospinning in only one study. As seen from TEM and SEM images of Yb_2O_3 produced

* Correspondence: adem.sarilmazz@gmail.com

within the scope of this study, the obtained nanomaterials formed as irregular nanoparticles rather than nanofiber [20]. In other nanofiber studies, ytterbium has been used as a dopant material in metal oxide nanofibers [21-24].

It has been understood from the literature review that the synthesis studies of Yb_2O_3 nanostructures are limited, and there is no report on the production of their well-crystallized nanofiber. The production of homogeneous and highly crystalline Yb_2O_3 nanofibers by electrospinning has been reported for the first time in this study. Moreover, a detailed bandgap analysis of Yb_2O_3 nanofiber has also been carried out. These band gap studies show that the obtained highly crystalline nanofibers can be an alternative to ZnO and TiO_2, which are used extensively in energy applications.

2. Materials and methods

2.1. Materials

Ytterbium(III) acetate hydrate ($YbAc_3$, 99.95%) and Polyacrylonitrile (PAN, Mw = 150 000 g mol^{-1}) were provided by Aldrich. *N, N*-Dimethylformamide (DMF) was supplied from Isolab.

2.2. Synthesis procedure of Yb_2O_3 nanofibers

Yb_2O_3 nanofibers were produced by the electrospinning technique in parallel with previous studies [25, 26]. Typically, 1 mmol $YbAc_3$ was dissolved in 5 mL DMF and then 400 mg PAN (8% w/v) was added to the solution. This mixture was stirred overnight to obtain a homogeneous solution. The homogenized solution was then placed in the syringe with a 21-gauge needle and the feed rate of the syringe pump was set as 1 mL/h.

The sample collector was fixed vertically opposite the syringe pump and its distance from the needle was adjusted to 15 cm. After the solution is prepared and the system requirements are set as described, voltage with 18 kV was applied to the metallic needle for the required electric field causing the formation of nanofibers and the sample collector was grounded. Thus, $YbAc_3$+PAN nanofibers were collected on aluminum foils on the sample collector and these nanofibers were calcined at 500 °C for 1 h. In this way, the polymer used as a template and other volatile substances in the environment were removed and Yb_2O_3 nanofibers were obtained. The process steps of this technique are shown schematically in Figure 1.

3. Results and discussions

First of all, powder X-ray diffraction (XRD) was employed as a bulk analysis technique to confirm the phase structure and purity of the Yb_2O_3 compound. Figure 2 demonstrates the XRD pattern of the Yb_2O_3 nanofibers. In this structure, the distinctive diffraction signals indicate that Yb_2O_3 has a cubic structure (JCPDS card no. 043-1037) with space group Ia-3. The unit cell of this structure consists of 44 polyhedra centered on Yb, and in this structure, each ytterbium atom bonds with 6 oxygen atoms (Figure 2).

The XRD results show that all diffraction peaks are smooth and intense. At the same time, the absence of peaks belonging to another phase structure confirmed the purity of the Yb_2O_3 nanofibers. Moreover, the crystallite size distributions were calculated from the XRD pattern by the modified Scherrer's equation and Williamson–Hall method, and the graphs of these measurements were given in the supplementary part (Figures S1 and S2). The crystallite size of the particles that make up the nanofibers was estimated as 6.53 nm and 6.74 nm by modified Scherrer's equation and Williamson–Hall method, respectively.

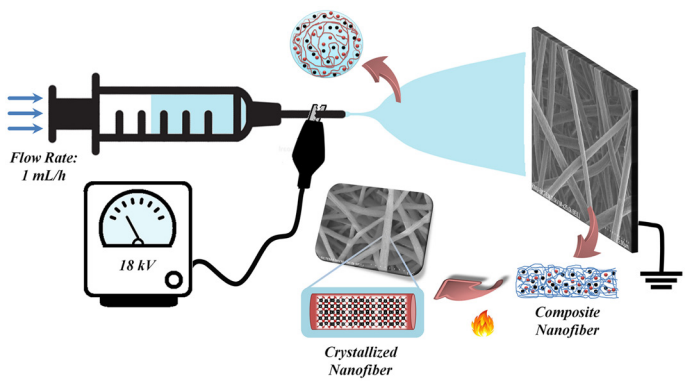

Figure 1. Schematic illustration of the production process of Yb_2O_3 nanofibers.

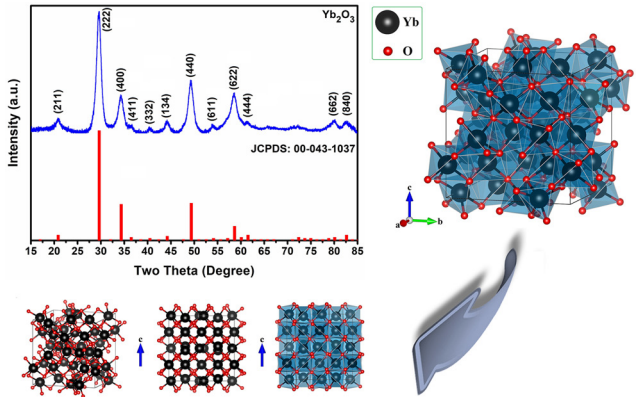

Figure 2. XRD pattern and 3D-crystal structures of the Yb_2O_3 nanofibers (these crystal structures were plotted with Vesta software).

Morphological, crystalline, and compositional properties of the nanofibers were studied by SEM, TEM, elemental mapping, and EDX characterization methods. SEM images of nanofibers pre- and postcalcination process were given in Figures 3a–3c, respectively. These results show that nanofibers have homogeneous size distribution. Moreover, it was determined that the diameters of precalcination nanofibers were 450 nm, and after the heat treatment, the diameters of the crystallized nanofibers decreased to 125 nm due to the loss of organic components. As a result of the performed measurements, the diameter distribution graphs of composite and crystalized nanofibers are given in Figures S3 and S4.

The morphological and crystal properties of nanofibers were detailed by TEM and HR-TEM analyses and the obtained results are given in Figures 3d–3f. It can be seen from the TEM images, the produced nanofibers have homogenous size distribution and this result is also consistent with the SEM results. Figure 3e clearly shows that the nanofibers consisted of Yb_2O_3 nanoparticles with about 9 ± 2 nm. Additionally, this measurement is compatible with crystallite size calculation from the XRD pattern by the modified Scherrer's equation and Williamson–Hall method. These nanoparticles, which are in contact with each other, were sintered with the effect of heat treatment and thus the nanofiber form was preserved.

The crystallinity of nanofibers was also investigated by the HR-TEM image given in Figure 3f. The perfectly and regular arrangement of the atoms indicates that the fabricated nanofibers have high crystallinity. Moreover, the performed calculations from the XRD pattern show that nanofibers have an 82.75% crystallinity percentage, and this estimate is compatible with TEM results. The process steps belonging to the determination of crystallinity percentage were explained in the supplementary part.

Furthermore, the interplanar spacing was calculated as 3.04 Å, and this value corresponds to the (222) crystallographic plane. In the XRD diffraction pattern, the most intense peak at 29.5° corresponds with the (222) plane, which indicates that the nanoparticles contained in the nanofibers are largely arranged in the (222) plane. Therefore, the obtained results from HR-TEM are compatible with XRD analysis. The elemental distribution and composition of the nanofibers were studied by elemental mapping and EDX analysis methods. Figures 4a–4c reveal that Yb and O elements were homogeneously distributed in the Yb_2O_3 nanofibers. Moreover, the chemical composition was calculated as $Yb_{2.19}O_{2.81}$ from the EDX spectrum (Figure 4d), and these values are quite close to theoretical ratios.

The chemical valance state of the nanofibers was analyzed by the XPS spectra. The high-resolution XPS spectra of Yb 4d and O 1s are given in Figure 5. Yb 4d signals were fitted with five singlet peaks by Gaussian profile (Figure 5a). The peaks centered at 184.4 and 198.8 eV were associated with spin-orbit-split $4d_{5/2}$ and $4d_{3/2}$, respectively, and satellite peaks were also detected at 192.4 and 205.3 eV. The energy difference of spin-orbit-split was found to be 14.4 eV as reported in the literature, and it was attributed to the 3+ valance state of Yb [27, 28]. In addition, the peak at 187.3 eV was correlated to the presence of ytterbium oxalate [29]. It was commented that ytterbium oxalate may have occurred from the reaction of $YbAc_3$ with organic molecules in the polymer due to the effect of applied temperature during the oxidation of nanofibers. The O 1s high-resolution spectra fitted to two singlet peaks was displayed in Figure 5b. As a result of performed fitting, it was determined that the peak centered at 529.1 was related to O^{2-} ions in the Yb_2O_3 crystal structure, while the peaks at 531.5 eV were caused by the hydroxyl group and oxygen vacancies [30].

The optical properties of nanofibers were investigated by diffuse reflectance spectra and their result is given in Figure 6a. According to this graph, nanofibers have weak reflectivity in the ultraviolet region, while this value increases

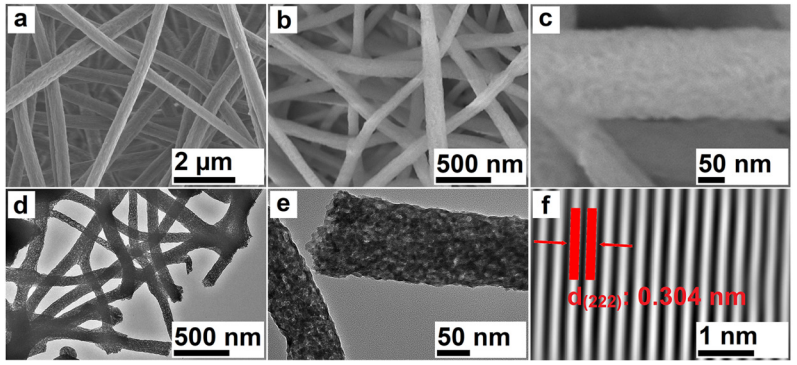

Figure 3. SEM (a–c), TEM (d,e), and HR-TEM (f) characterization results of $YbAc_3$+PAN (a) and Yb_2O_3 (b–f) nanofibers (particle size and fiber diameter were measured by using ImageJ).

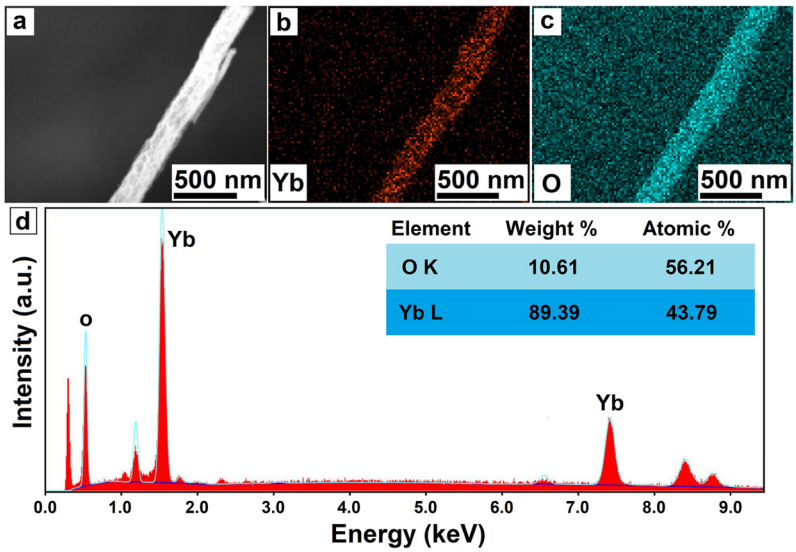

Figure 4. SEM image where EDX and elemental mapping analyses were carried out (a). elemental mapping (b,c), and EDX (d) results of Yb_2O_3 nanofibers.

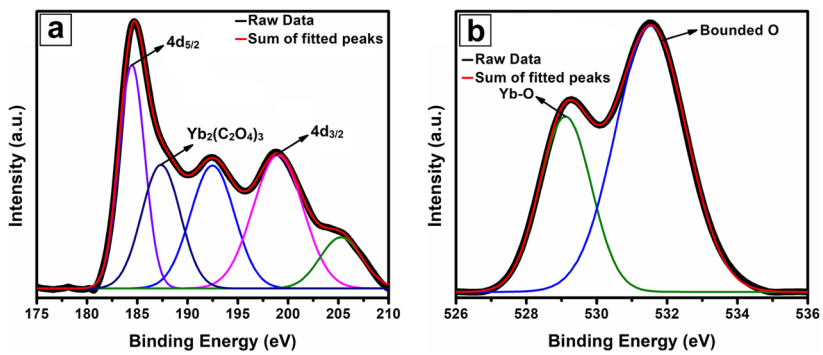

Figure 5. The high resolution XPS spectrum of Yb 4d (a) and O1s (b).

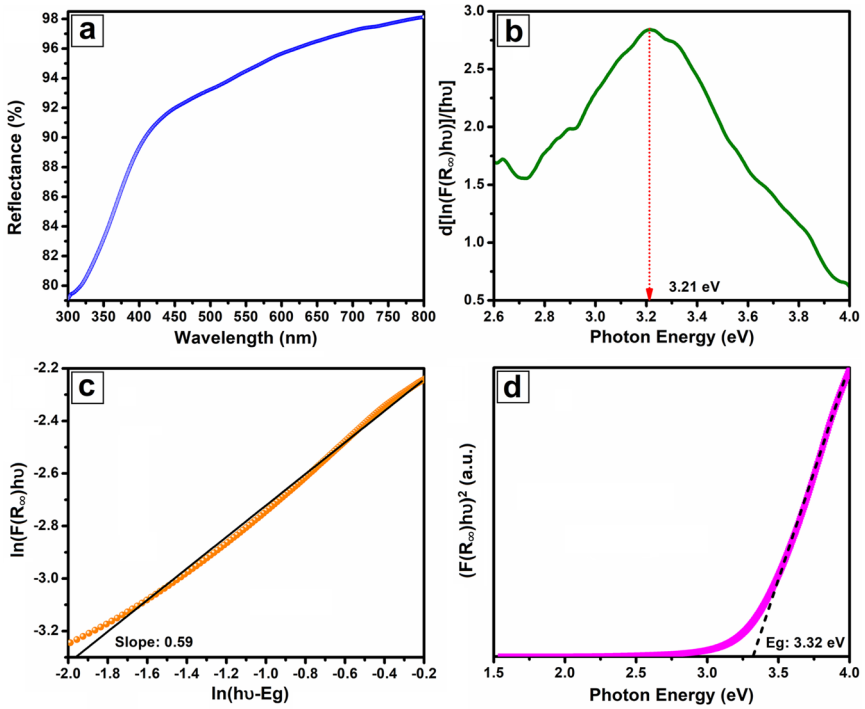

Figure 6. Diffuse reflectance (a), d[ln(F(R_∞)hυ)]/[hυ] vs. photon energy graph (b), ln(F(R_∞)hυ) vs. ln(hυ-E_g) graph (c), and band-gap energy diagram (d) of Yb_2O_3 nanofibers.

towards the visible part and reaches a maximum in the near-infrared region. The obtained data from diffuse reflectance spectroscopy were used to calculate the band-gap and determine its type. Firstly, the absorption (F(R_∞)) was calculated from the Kubelka–Munk equation given in Equation 1.

$$F(R_\infty) = \frac{(1-R)^2}{(2R)} \quad \text{Equation 1}$$

where $F(R_\infty)$ is absorption and R is reflection.

The absorption value was used to estimate the approximately band-gap (3.21 eV), which is determined by the graph of d[ln(F(R_∞)hυ)]/d[hυ]-hυ (Figure 6b). The m exponent was assigned from the slope of the ln(F(R_∞)hυ)-ln(hυ-Eg) plot (Figure 6c) obtained from Tauc's equation (Equation 2). The m value was calculated as 0.6 and this shows that Yb_2O_3 nanofibers have direct transition type [31, 32].

$$F(R_\infty)h\upsilon = A(h\upsilon - E_g)^m \quad \text{Equation 2}$$

where hv is photon energy, A is energy-independent constant, Eg is optical band gap and m is exponent a value that determines bandgap types.

The optical band-gap of nanofibers was estimated as 3.32 eV by fitting the linear part of the graph of $(F(R_\infty)h\upsilon)^2$ vs photon energy given in Figure 6d.

FTIR spectroscopy was carried out to determine the presence of organic molecules in crystalized Yb_2O_3 nanofibers. FTIR results of crystalized nanofiber, polymer composite, and PAN are given comparatively in Figure 7. The FTIR results of PAN and composite nanofibers show that the characteristic peaks at 2935, 2245, 1448, 1360, 1242, and 1072 cm^{-1} are matched to the bond vibration of organic molecules belonging to PAN. The bands at 2935, 2245, and 1448 cm^{-1} were attributed to stretching of the C-H of the CH_2, the C≡N of the acrylonitrile group, and the C=O of the carbonyl group, respectively. The peak centered at 1448 cm^{-1} occurred from CH_2 tensile vibration, while the peak at 1360 cm^{-1} was ascribed to the C-H stretching of aliphatic CH groups. Furthermore, the C-H and C-O bond vibrations were observed at 1242 and 1072 cm^{-1}, respectively [33, 34]. After the calcination process, these characteristic peaks of PAN disappeared due to the decomposition of organic molecules under the influence of heat treatment. Moreover, the peak at 568 cm^{-1} which is seen in the FTIR result of Yb_2O_3 nanofibers was assigned to bond vibration between Yb with O atoms.

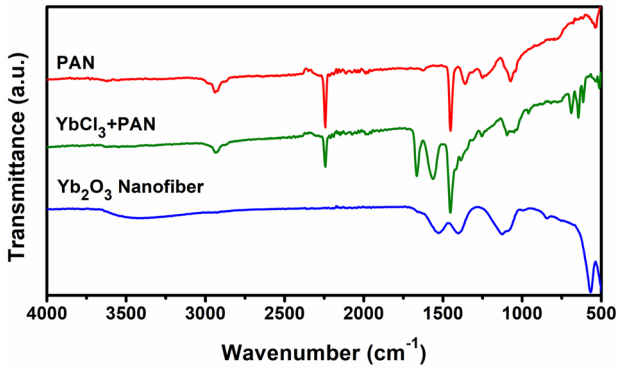

Figure 7. FTIR spectra results of Yb_2O_3, $YbAc_3$+PAN nanofibers, and PAN.

4. Conclusion

Highly crystalline, pure, and homogeneous Yb_2O_3 nanofibers were fabricated by the electrospinning technique and presented to the literature for the first time with this study. The produced nanofibers were characterized by various methods such as XRD, SEM, TEM, elemental mapping, EDX, XPS, UV-Vis spectroscopy, and FTIR. As a result of the analyses, it was seen that the nanofibers consist of nanoparticles with 9 ± 2 nm, which have a pure and cubic crystal structure. Moreover, the chemical composition of the nanofibers was calculated as $Yb_{2.19}O_{2.81}$ by EDX. It was determined with optical measurements and calculations that the nanofibers have a direct band transition type and a band-gap value of 3.32 eV. The obtained characterization results show that the high crystalline Yb_2O_3 nanofibers can be used in many energy applications such as solar cells, hydrogen production, oxygen evolution-reduction reactions, and fuel cells. Moreover, it is predicted that produced nanofibers may contribute to an increase in application efficiencies because they have a larger contact surface area than other nanomaterials with different morphology used in these applications.

Supporting Information

The particle size distribution was estimated by modified Scherrer equation and Williamson–Hall method which are given in the supporting information.

References

1. Gui ZZ, Liu X, Ming S, Zhang JY, Xie Q et al. Efficient organic solar cells employing ytterbium ion-doped zinc oxide as cathode transporting layer. Organic Electronics 2018; 53: 296-302. https://doi.org/10.1016/j.orgel.2017.11.008
2. Morassaei MS, Salehabadi A, Salavati-Niasari M, Akbari A. Preparation, structural analysis, and assessing the impacts of holmium and ytterbium on electrochemical hydrogen storage property of strontium cerium molybdate nanostructures. Electrochimica Acta 2020; 356: 136851. https://doi.org/10.1016/j.electacta.2020.136851
3. Cots A, Gómez R. Ytterbium modification of pristine and molybdenum-modified hematite electrodes as a strategy for efficient water splitting photoanodes. Applied Catalysis B: Environmental 2017; 219: 492-500. https://doi.org/10.1016/j.apcatb.2017.07.067
4. Gonell F, Haro M, Sánchez RS, Negro P, Mora-Seró I et al. Photon up-conversion with lanthanide-doped oxide particles for solar H2 generation. The Journal of Physical Chemistry C 2014; 118 (21): 11279-11284. https://doi.org/10.1021/jp503743e
5. Leduc J, Gönüllü Y, Raauf A, Fischer T, Mathur S. Chapter five-rare-earth-containing materials for photoelectrochemical water splitting applications. In: Mi Z,Wang L, Jagadish C (Editors). Semiconductors and Semimetals. Elsevier, 2017, pp. 185-219. https://doi.org/10.1016/bs.semsem.2017.05.001
6. Cheng L, Xu X, Fang Y, Li Y, Wang J et al. Triblock copolymer-assisted construction of 20 nm-sized ytterbium-doped TiO2 hollow nanostructures for enhanced solar energy utilization efficiency. Science China Chemistry 2015; 58 (5): 850-857. https://doi.org/10.1007/s11426-014-5237-1
7. Sordello F, Berruti I, Gionco C, Paganini MC, Calza P et al. Photocatalytic performances of rare earth element-doped zinc oxide toward pollutant abatement in water and wastewater. Applied Catalysis B: Environmental 2019; 245: 159-166. https://doi.org/10.1016/j.apcatb.2018.12.053

8. Cerrato E, Zickler GA, Paganini MC. The role of Yb doped ZnO in the charge transfer process and stabilization. Journal of Alloys and Compounds 2020; 816: 152555. https://doi.org/10.1016/j.jallcom.2019.152555

9. He Y, Chen M, Jiang Y, Tang L, Yu J et al. Tubular g-C3N4 coupled with lanthanide oxides Yb2O3 as a novel bifunctional photocatalyst：Enhanced photocatalytic NO removal and H2 evolution, dual regulation and reaction pathway. Journal of Alloys and Compounds 2022; 903: 163806. https://doi.org/10.1016/j.jallcom.2022.163806

10. Sewell RH, Clark A, Smith R, Semans S, Jamora A et al. Silicon solar cells with monolithic rare-earth oxide upconversion layer. In IEEE Photovoltaic Specialists Conference 34; Philadelphia, PA, USA; 2009. pp. 002448-002453. https://doi.org/10.1109/PVSC.2009.5411287

11. Muthulakshmi V, Sundrarajan M. Green synthesis of ionic liquid assisted ytterbium oxide nanoparticles by Couroupita guianensis abul leaves extract for biological applications. Journal of Environmental Chemical Engineering 2020; 8 (4): 103992. https://doi.org/10.1016/j.jece.2020.103992

12. Ibrahim AA, Ahmad R, Umar A, Al-Assiri MS, Al-Salami AE et al. Two-dimensional ytterbium oxide nanodisks based biosensor for selective detection of urea. Biosensors and Bioelectronics 2017; 98: 254-260. https://doi.org/10.1016/j.bios.2017.06.015

13. Khairy M, Banks CE. A screen-printed electrochemical sensing platform surface modified with nanostructured ytterbium oxide nanoplates facilitating the electroanalytical sensing of the analgesic drugs acetaminophen and tramadol. Microchimica Acta 2020; 187 (2): 126. https://doi.org/10.1007/s00604-020-4118-x

14. Hosokawa S, Iwamoto S, Inoue M. Synthesis of nesoporous needle-shaped ytterbium oxide crystals by solvothermal treatment of ytterbium chloride. Journal of the American Ceramic Society 2007; 90 (4): 1215-1221. https://doi.org/10.1111/j.1551-2916.2007.01611.x

15. Jiang X, Yu L, Yao C, You F, Zhang J. Facile fabrication and characterization of ytterbium oxide hollow spheres using carbon spheres as template. Nano 2016; 11 (06): 1650067. https://doi.org/10.1142/S1793292016500673

16. Rahimi-Nasrabadi M, Pourmortazavi SM, Aghazadeh M, Ganjali MR, Karimi MS et al. Fabrication, characterization and photochemical activity of ytterbium carbonate and ytterbium oxide nanoparticles. Journal of Materials Science: Materials in Electronics 2017; 28 (13): 9478-9488. https://doi.org/10.1007/s10854-017-6691-2

17. Xiao Y, Han G, Chang Y. Electrospun ytterbium and europium ions co-doped stannic oxide nanofibers and application in dye-sensitized solar cells. Materials Research Bulletin 2017; 92: 90-98. https://doi.org/10.1016/j.materresbull.2017.04.017

18. Choi, SK, Kim S, Lim SK, Park H. Photocatalytic comparison of TiO2 nanoparticles and electrospun TiO2 nanofibers: Effects of mesoporosity and interparticle charge transfer. The Journal of Physical Chemistry C 2010; 114 (39): 16475-16480. https://doi.org/10.1021/jp104317x

19. Liu H, Yang J, Liang J, Huang Y, Tang C. ZnO nanofiber and nanoparticle synthesized through electrospinning and their photocatalytic activity under visible light. Journal of the American Ceramic Society 2008; 91 (4): 1287-1291. https://doi.org/10.1111/j.1551-2916.2008.02299.x

20. Henriques MS, Ferreira AC, Cruz A, Ferreira LM, Branco JB et al. Preparation of Yb2O3 submicron- and nano-materials via electrospinning. Ceramics International 2015; 41 (9, Part A): 10795-10802. https://doi.org/10.1016/j.ceramint.2015.05.017

21. Cacciotti I, Bianco A, Pezzotti G, Gusmano G. Terbium and ytterbium-doped titania luminescent nanofibers by means of electrospinning technique. Materials Chemistry and Physics 2011; 126 (3): 532-541. https://doi.org/10.1016/j.matchemphys.2011.01.034

22. Ge W, Shi J, Xu M, Chen X, Zhu J. Red upconversion luminescence (UCL) properties in one-dimensional Yb2Ti2O7:Er nanofibers via an electrospinning route. Journal of Alloys and Compounds 2019; 788: 993-999. https://doi.org/10.1016/j.jallcom.2019.02.319

23. Liao F, Chu LF, Guo CX, Guo YJ, Ke QF et al. Ytterbium doped TiO2 nanofibers on activated carbon fibers enhances adsorption and photocatalytic activities for toluene removal. ChemistrySelect 2019; 4 (31): 9222-9231. https://doi.org/10.1002/slct.201902002

24. Han L, Hu Y, Pan M, Xie Y, Liu Y et al. A new tactic to achieve Y2O2S:Yb3+/Er3+ up-conversion luminescent hollow nanofibers. CrystEngComm 2015; 17 (12): 2529-2535. https://doi.org/10.1039/C4CE02527J

25. Rüşen A, Topçu MA, Sarilmaz A, Özel F. Fabrication and characterization of electrospun single-crystal lead manganese borate nanofibers. Materials Research Bulletin 2018; 99: 249-254. https://doi.org/10.1016/j.materresbull.2017.11.026

26. Yanalak G, Aljabour A, Aslan E, Ozel F, Patir IH et al. NiO and Co3O4 nanofiber catalysts for the hydrogen evolution reaction at liquid/liquid interfaces. Electrochimica Acta 2018; 291: 311-318. https://doi.org/10.1016/j.electacta.2018.08.130

27. Ugendar K, Samanta S, Rayaprol S, Siruguri V, Markandeyulu G et al. Effect of frustrated exchange interactions and spin-half-impurity on the electronic structure of strongly correlated NiFe2O4. Physical Review B 2017; 96 (3): 035138. https://doi.org/10.1103/PhysRevB.96.035138

28. López-Mena ER, Ceballos-Sanchez O, Hooper TJN, Sanchez-Ante G, Rodríguez-Muñoz M et al. The effect of Yb doping on ZnO thin films obtained via a low-temperature spin coating method. Journal of Materials Science: Materials in Electronics 2021; 32 (1): 347-359. https://doi.org/10.1007/s10854-020-04785-7

29. Uwamino Y, Ishizuka T, Yamatera H. X-ray photoelectron spectroscopy of rare-earth compounds. Journal of Electron Spectroscopy and Related Phenomena 1984; 34 (1): 67-78. https://doi.org/10.1016/0368-2048(84)80060-2

30. Kahraman A, Karacali H, Yilmaz E. Impact and origin of the oxide-interface traps in Al/Yb2O3/n-Si/Al on the electrical characteristics. Journal of Alloys and Compounds 2020; 825: 154171. https://doi.org/10.1016/j.jallcom.2020.154171

31. Sarilmaz A, Yanalak G, Aslan E, Ozel F, Patir IH et al. Shape-controlled synthesis of copper based multinary sulfide catalysts for enhanced photocatalytic hydrogen evolution. Renewable Energy 2021; 164: 254-259. https://doi.org/10.1016/j.renene.2020.09.052

32. Makuła P, Pacia M, Macyk W. How to correctly determine the band gap energy of modified semiconductor photocatalysts based on UV–Vis spectra. The Journal of Physical Chemistry Letters 2018; 9 (23): 6814-6817. https://doi.org/10.1021/acs.jpclett.8b02892

33. Yang C, Wang B, Zhang Y, Wang H. Preparation and properties of polyacrylonitrile fibers with guanidine groups. Fibers and Polymers 2015; 16 (8): 1611-1617. https://doi.org/10.1007/s12221-015-4480-1

34. Mahmood HS, Jawad MK. Antibacterial activity of chitosan/PAN blend prepared at different ratios. In: AIP Conference Proceedings 2190 (1); Athens, Greece; 2019. pp. 020078. https://doi.org/10.1063/1.5138564

Supporting Information

Percentage of crystallinity

The percent crystallinity of nanofibers was calculated from the XRD pattern using the following equation.

$$X_c = \frac{A_c}{A_c + A_a} \text{X } 100$$

where X_c is the degree of crystallinity, A_c and A_a are the areas of crystalline and amorphous peaks in the XRD pattern, respectively.

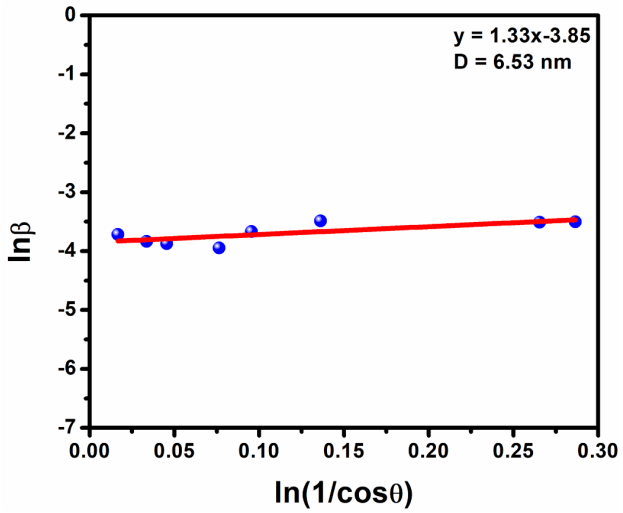

Figure S1. Modified Sherrer method graph of Yb_2O_3 porous nanofibers.

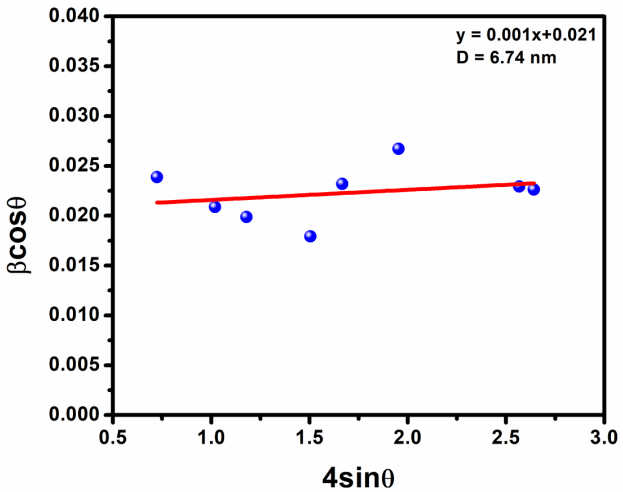

Figure S2. Williamson–Hall method graph of Yb_2O_3 porous nanofibers.

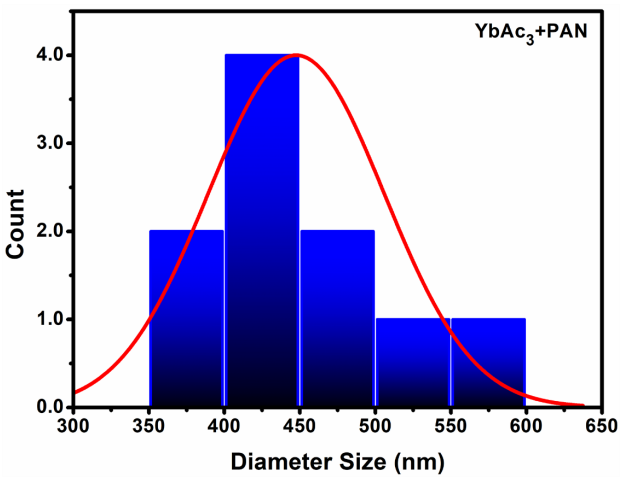

Figure S3. Diameter size distribution graph of $YbAc_3$+PAN composite nanofibers.

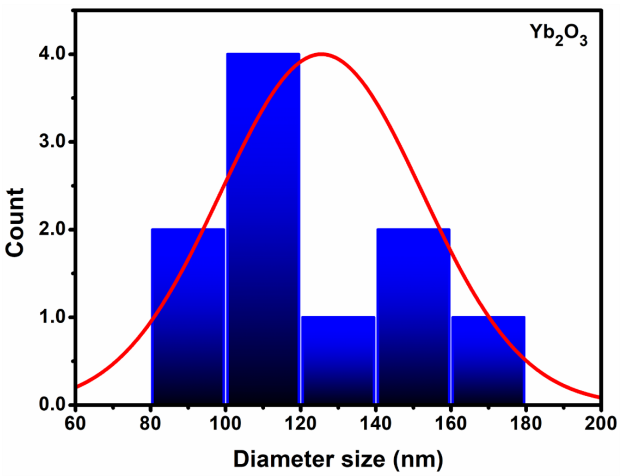

Figure S4. Diameter size distribution graph of Yb_2O_3 nanofibers.